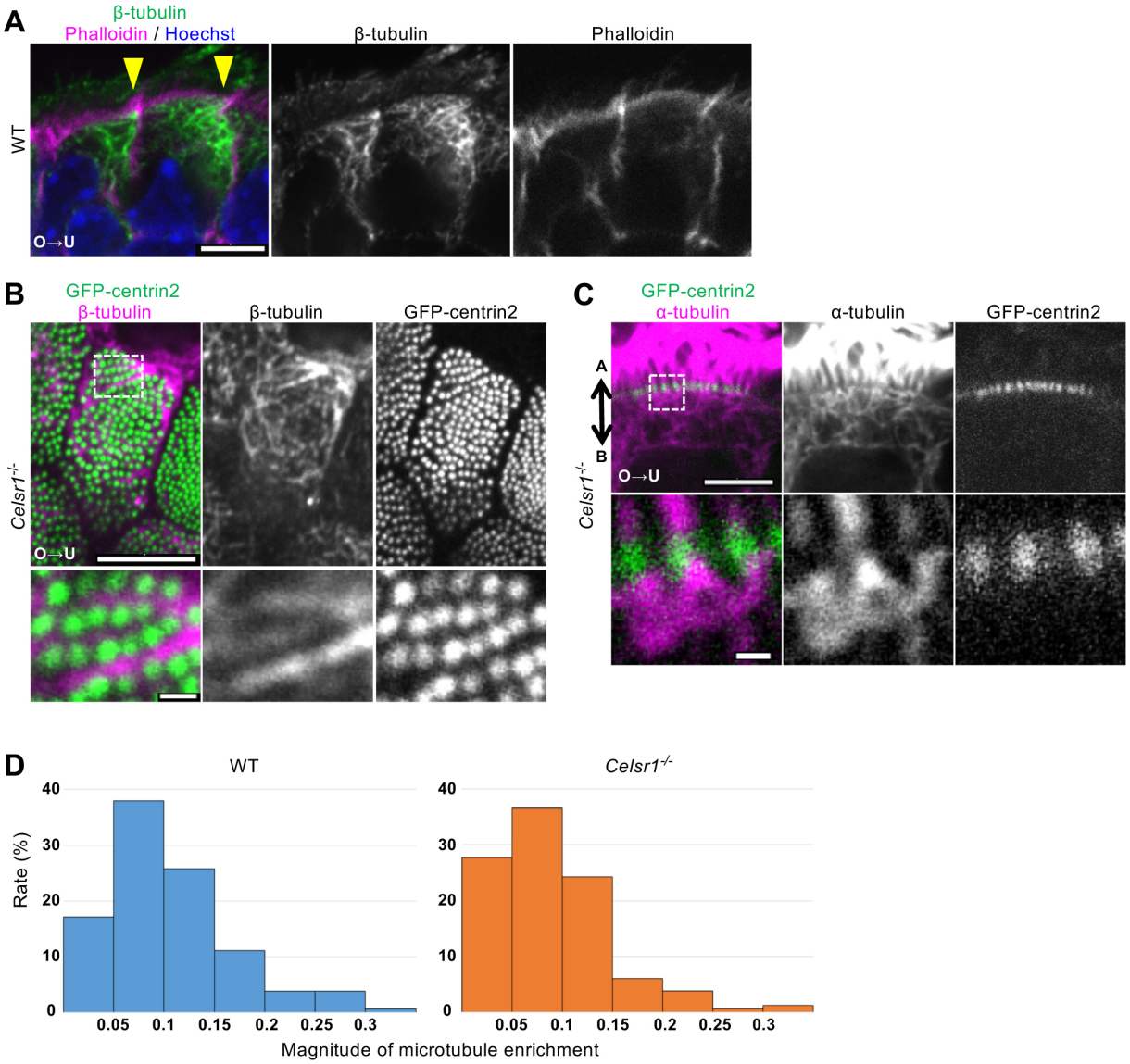

Fig. S1, Microtubule organization was maintained in *Celsr1*$^{-/-}$ MCC
A, Lateral view of WT MCCs stained with anti-β-tubulin (green) and phalloidin (magenta). Arrowheads indicate cell-cell boundary identified by phalloidin signals. (Bar = 5 μm) B and C, Apical (B) and lateral view (C) of MCCs of *Celsr1*$^{-/-}$*; GFP-CETN2* transgenic mice stained with anti-β-tubulin (magenta in B) or anti-α-tubulin antibodies (magenta in C). The ovarian and uterine side are on the left and right, respectively in all images (shown as O > U). B, Top row, MIP image was rendered from three images acquired at a step size of 0.2 μm. Bottom row shows high magnification images of a single plane. C, Single plane images. Bottom row, high magnification. Apical is to the top of the images. (Bar = 5 μm and 0.5 μm in the top and bottom rows, respectively, in both B and C.) D, Histograms show the results of quantifying the magnitude of microtubule enrichment near the cell-cell boundary in WT and *Celsr1*$^{-/-}$ MCCs. The lower the value of the magnitude, the more uniform the distribution of microtubules. The same samples shown in Fig. 2 B and B' are used. 369 cells and 347 cells in WT and *Celsr1*$^{-/-}$ tissues, respectively, were used for the analysis.

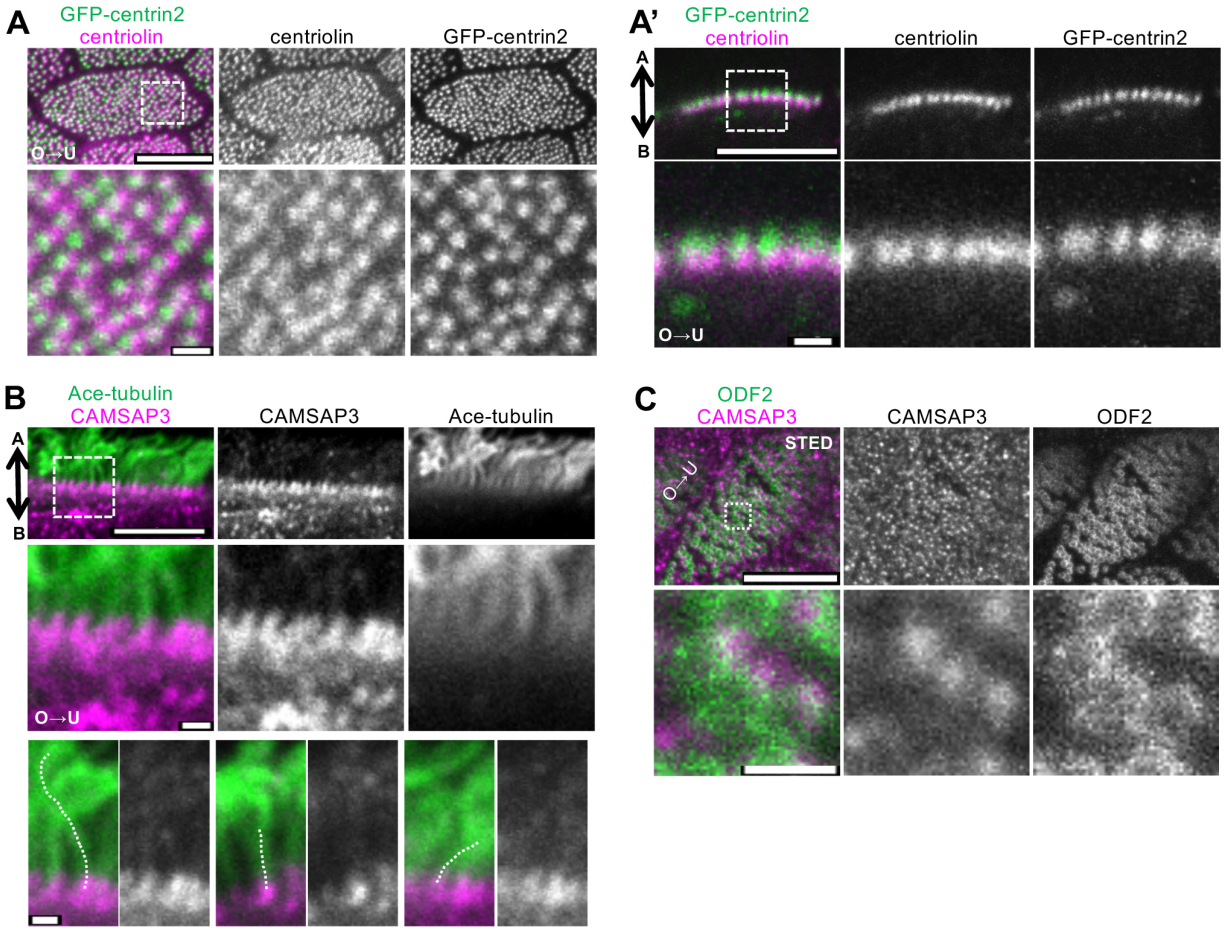

Fig. S2, Localization of BB related proteins

A and A', Apical (A) and lateral (A') views of the oviduct expressing GFP-centrin2 (green) stained with anti-centriolin (magenta) antibody. MIP images rendered from 5 images acquired at a step size of 0.2 μm (A), and single plane images (A'). Lower panels show magnified views of the boxed region in the upper panel. (Bar = 5 μm (top), = 0.5 μm (bottom)) B, Lateral view of adult WT oviduct stained with anti-CAMSAP3 (magenta), and anti-acetylated tubulin (green) antibodies. Middle panels show magnified images of the boxed region in the upper panel. Bottom panels show cilia (dotted lines) standing with different angles from the apical surface. (Bar = 5 μm (top panels), 0.5 μm (middle panels), and 0.5 μm (bottom panels)) C, Super resolution images (obtained by STED) of WT oviduct stained with anti-CAMSAP3 (magenta) and anti-ODF2 (green) antibodies. MIP image was rendered from three images acquired at a step size of 0.2μm. Bottom panels show the magnified images. (Bar = 5 μm (top) and 0.5 μm (bottom))

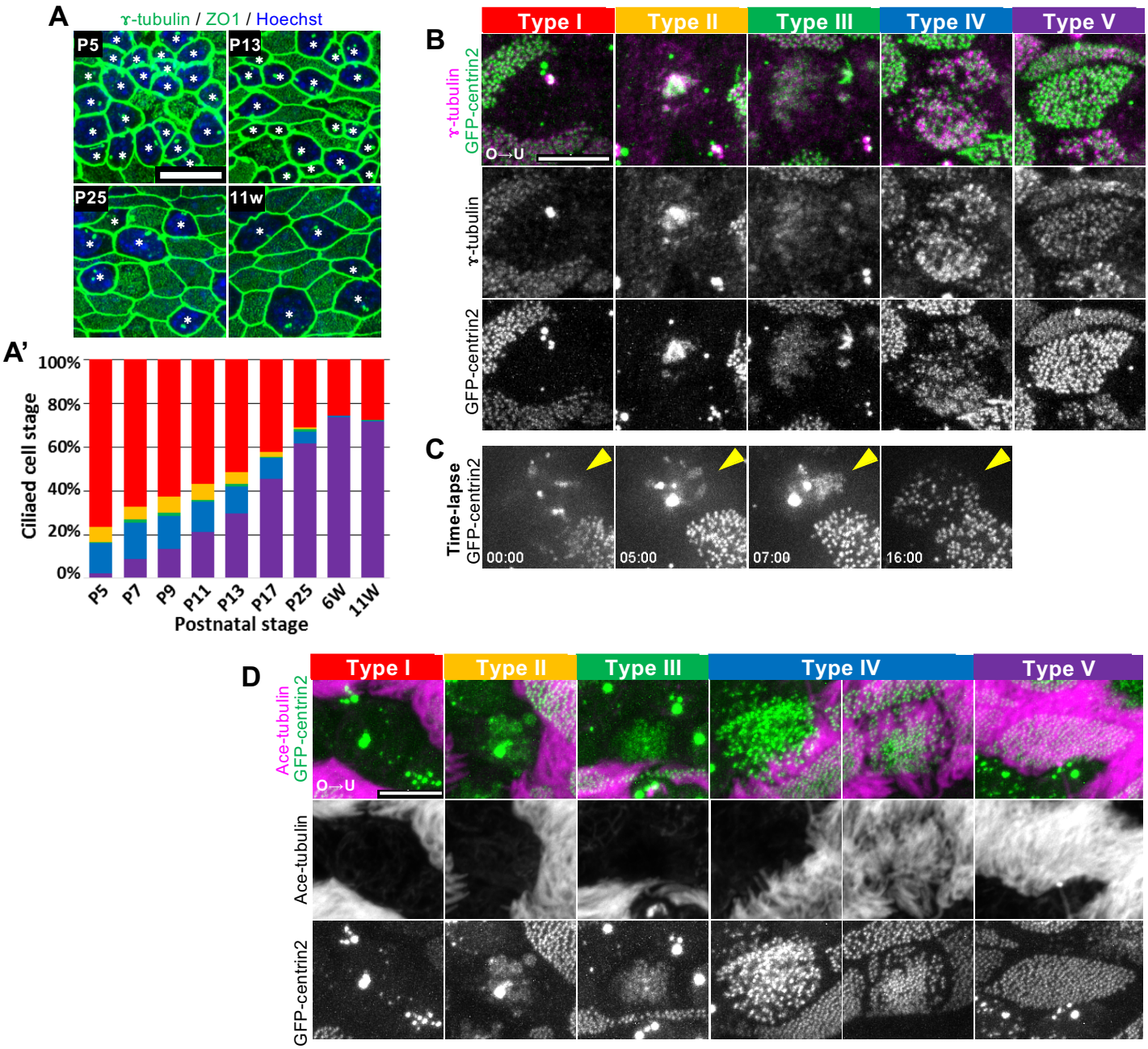

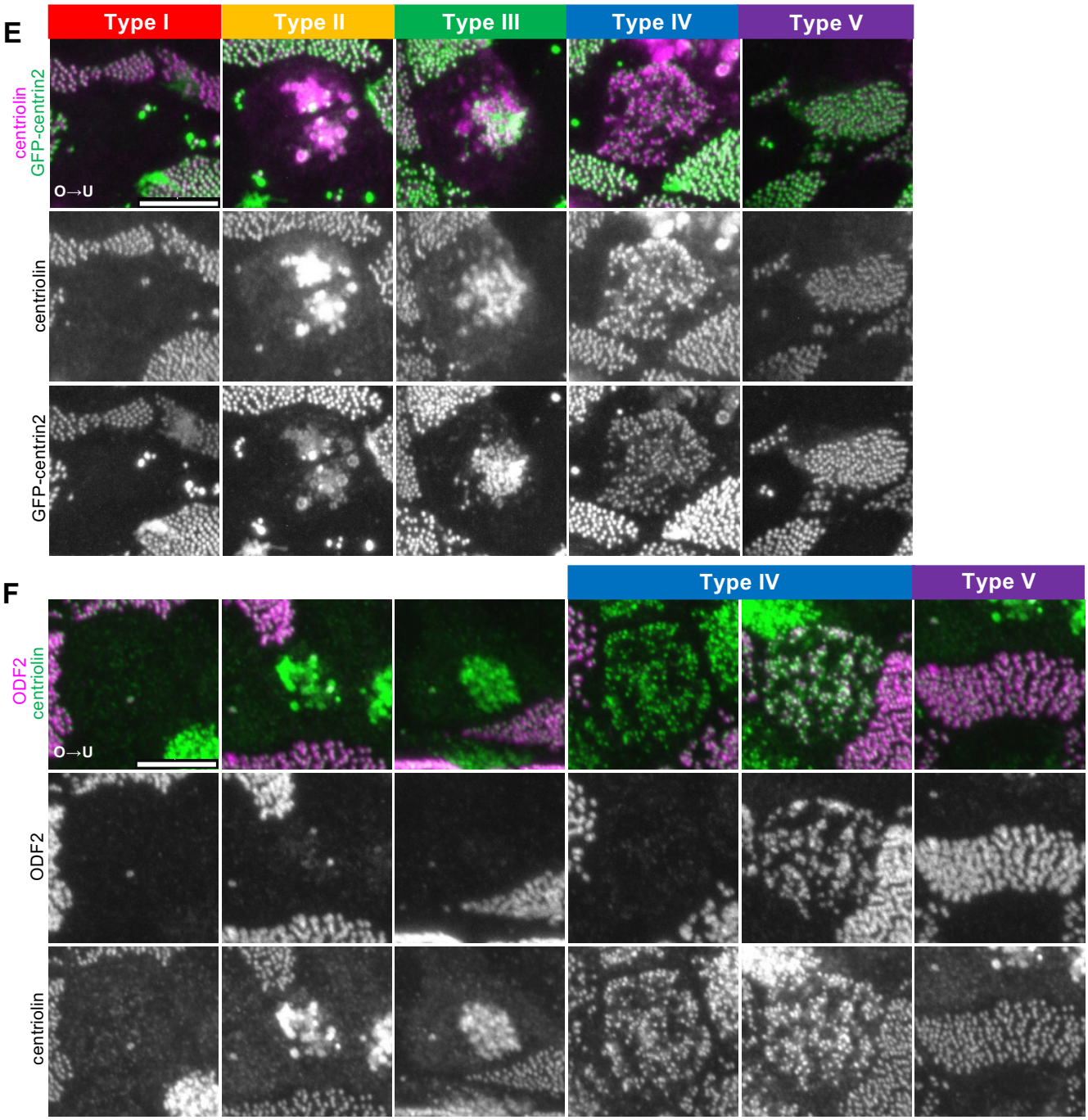

Fig. S3, Cell type transition and localization of BB proteins during the maturation process of oviduct MCCs

A, Representative images of oviducts on postnatal day 5 (P5) to 11 weeks (11w) stained with anti-ZO1 (green), anti-γ-tubulin (green), and Hoechst (blue). Secreting cells (which are categorized as type I) are shown with asterisks. (Bar = 10 μm) A', Changes in cell type composition at each developmental stage. Oviducts from three animals were used for the analysis. Analyzed cell numbers; 1469 (P5), 2341 (P7), 1999 (P9), 1609 (P11), 1791 (P13), 2077 (P17), 2807 (P25), 2493 (6w), and 2870 (11w). B, Confocal images of the oviduct expressing GFP-centrin2 (green) stained with anti-γ-tubulin (magenta). MIP images were rendered from 30 images acquired at a step size of 0.2 μm. (Bar = 5 μm) C, Snapshot images after time-lapse recording (same as Sup. Mov. 2) of *GFP-CETN2* oviduct. Arrowheads indicate the cell of interest undergoing cell type transition. Timepoints are shown on the bottom. D, Confocal images of the P13 oviduct expressing GFP-centrin2 (green) stained with anti-acetylated tubulin antibody (magenta). MIP images rendered from 50 slices acquired at a step size of 0.2 μm. (Bar = 5 μm) E, Confocal images of the P13 oviduct expressing GFP-centrin2 (green) stained with anti-centriolin antibody (magenta). MIP images rendered from 30 slices acquired at a step size of 0.2 μm. To compare signal intensities between cell types, all the images were cropped after simultaneously acquired images. F, Confocal images of P13 WT oviduct stained with anti-centriolin (green) and anti-ODF2 (magenta) antibodies. MIP images rendered from 30 slices acquired at a step size of 0.2 μm. All the images were cropped after from simultaneous acquisition. Two representative type IV cells with different ODF2 staining patterns are shown. ODF2 localized to BBs in 83% (183/221) of type IV cells and 100% of type V cells. (Bar = 5 μm)

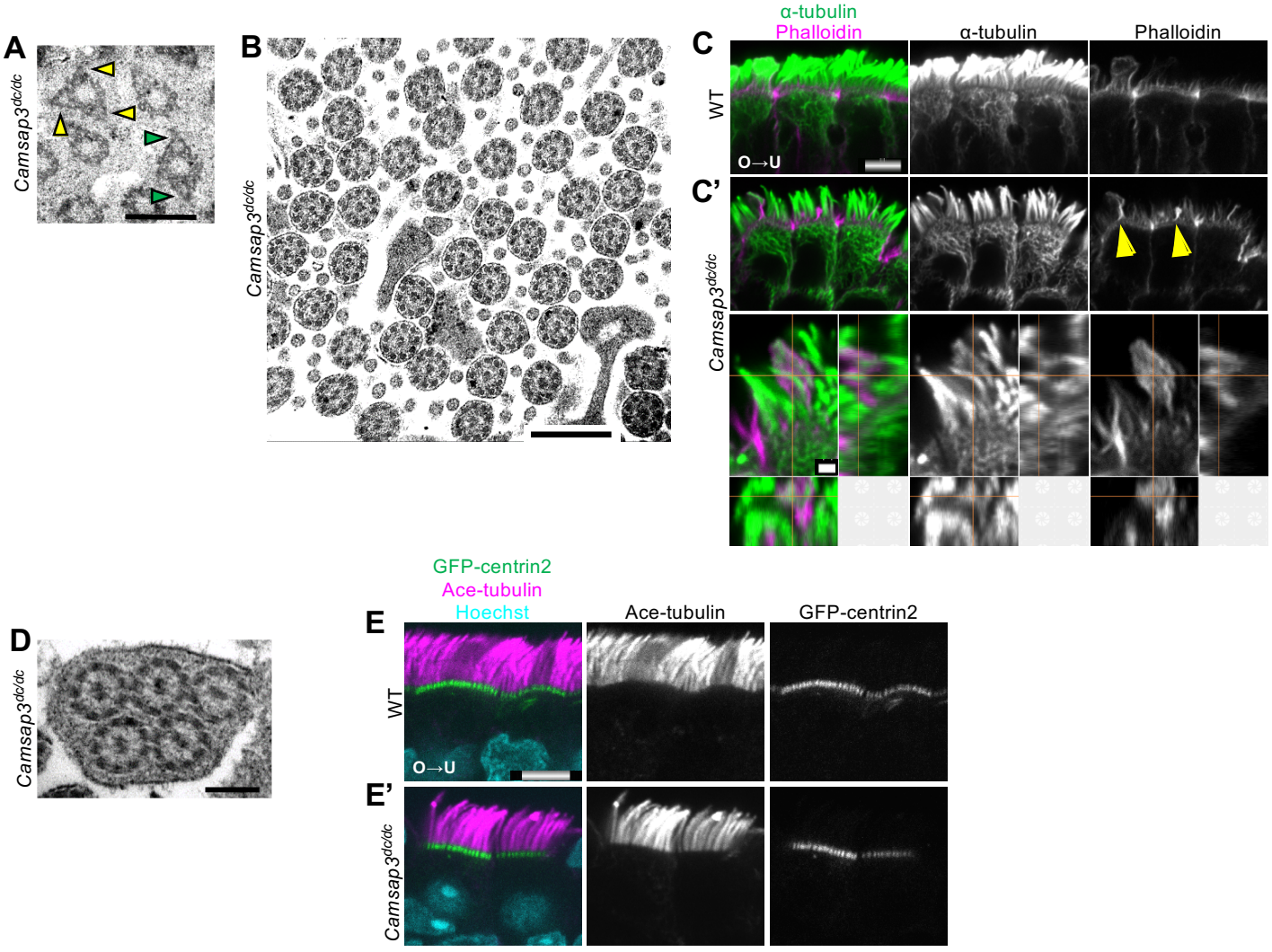

Fig. S4, Distribution of microtubules in *Camsap3*$^{dc/dc}$ mutant MCCs
A, Images of BBs observed with a transmission electron microscopy showing examples of abnormal BBs with multiple protrusions resembling BF (shown with arrow heads). High magnified image of Fig. 5E. (Bar = 0.5 μm) B, Electron micrograph of axonemes in a *Camsap3*$^{dc/dc}$ oviduct MCC. Central pair microtubules were observed in all the axonemes. C and C', Lateral view of oviducts of WT (C) and *Camsap3*$^{dc/dc}$ (C') stained with anti-α-tubulin antibody (green) and phalloidin (magenta). Bottom rows of (C') show 3D orthogonal views of abnormal protrusions with phalloidin signals (indicated with arrowheads). (Bar = 5 μm (top) and 1 μm (bottom)) D, Electron micrograph of abnormal cilia. Multiple axonemes within the same ciliary membrane. (Bar = 0.2 μm) E and E', Lateral view of MCCs of WT and *Camsap3*$^{dc/dc}$ animals with GFP-centrin2 (green) stained with anti-acetylated tubulin antibody (magenta) and Hoechst (cyan). (Bar = 5 μm)

A

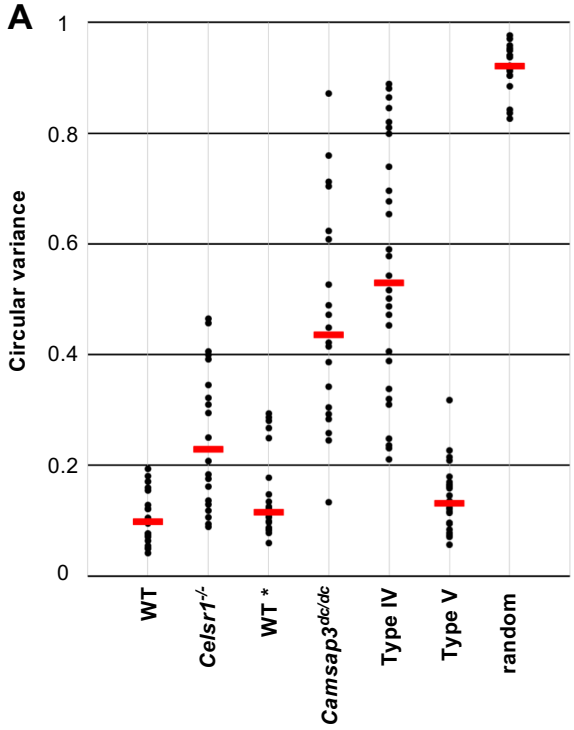

B

	WT	*Celsr1*$^{-/-}$	WT*	*Camsap3*$^{dc/dc}$	Type IV	Type V	random
WT							
Celsr1$^{-/-}$	0.002						
WT*	0.503	0.046					
Camsap3$^{dc/dc}$	2.77E-06	0.015	2.32E-05				
Type IV	9.98E-08	2.00E-04	1.13E-06	0.844			
Type V	0.298	0.039	1	1.01E-06	5.88E-09		
random	1.32E-06	1.32E-06	1.32E-06	2.07E-06	4.94E-07	9.98E-08	

Fig. S5, Statistical comparison of CVs in MCCs between genotypes and cell types

A, Data sets from Fig. 1D, 4E, and 5C were summarized for comparison. The distribution of CVs in MCCs is shown. Each point on the graph corresponds to one cell. Red line represents the median CV in each category (WT: 0.098, *Celsr1*$^{-/-}$: 0.23, WT*: 0.11, *Camsap3*$^{dc/dc}$: 0.44, Type IV: 0.53, Type V: 0.13, random: 0.92). "WT" and "*Celsr1*$^{-/-}$" show results of the 12 w old (same data as shown in Fig. 1D, n = 20 cells). "WT*" and "*Camsap3*$^{dc/dc}$," results of adult littermates (shown in Fig. 5C, n = 20 cells in WT and *Camsap3*$^{dc/dc}$). "Type IV" and "Type V," results of WT P13 (shown in Fig. 4E, n= 28 cells in each cell type). "random" is the result of a calculation using random numbers corresponding to 150 BBs, n = 20 cells. B, A table showing P values after the comparison between two groups. Non-parametric multiple comparisons were performed using the Steel-Dwass method. *p* values smaller than 0.05 are shown in orange.

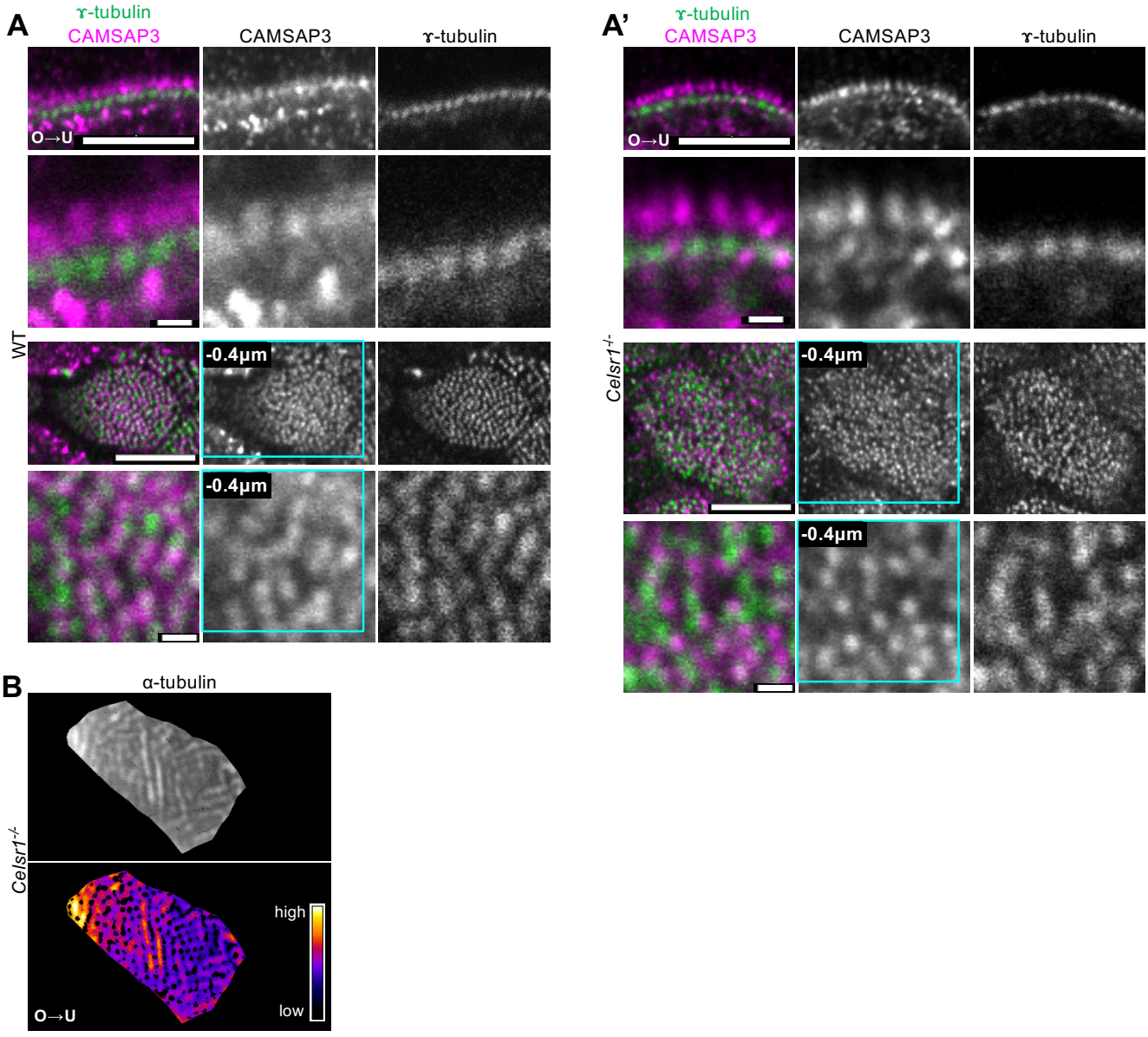

Fig. S6, CAMSAP3 localization to the base of cilia is maintained in *Celsr1*$^{-/-}$ mutant
A and A', WT and *Celsr1*$^{-/-}$ mutant (adult) MCCs stained with anti-CAMSAP3 (magenta) and anti-γ-tubulin (green) antibodies; lateral view (top rows) and apical view (bottom rows). All images were single plane. The focal plane of CAMSAP3 was 0.4 μm apical to the focal plane of γ-tubulin, and is indicated as "-0.4 μm" (cyan frame). Bottom panels show the magnified images. (Bar = 5 μm (top) and 0.5 μm (bottom)) B, Reconstructed images of α-tubulin signals located at the level of GFP-centrin2 signals in *Celsr1*$^{-/-}$ mutant. The same representation with Fig. 6F and F'. Intensity of signals were color-coded as shown in the bottom right inset. Position of GFP-centrin2 signals were masked to highlight the distribution of microtubules between BBs.

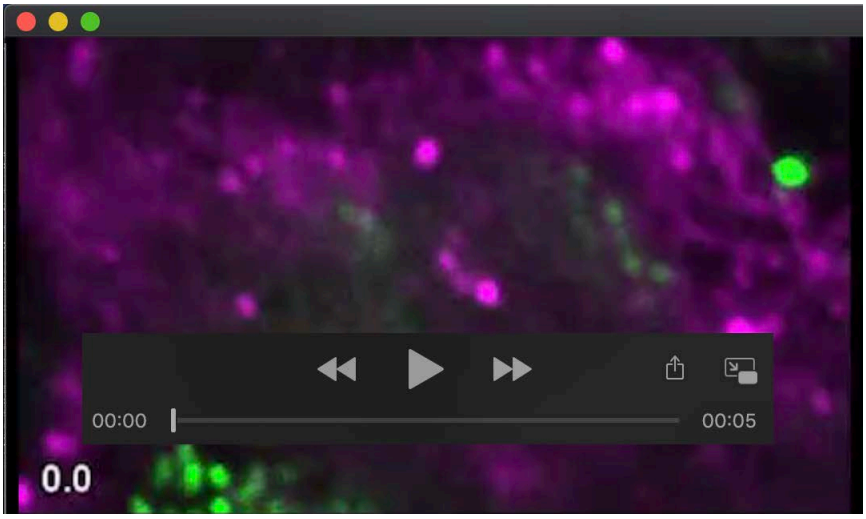

Movie 1, Confocal microscopy images of tubulin in a MCC along the apical-basal axis
GFP-centrin2 (green) and β-tubulin (magenta) in an oviduct MCC (the same cell shown in Fig. 2D). From apical to basal, the z-step size (0.2 μm) is shown on the bottom.

Movie 2, Time-lapse observation of MCC maturation
Time-lapse recording of a cell expressing GFP-centrin2. Snapshots are shown in Fig. S3C. The timepoint is indicated at the bottom (in hours). MIP images were rendered from micrographs acquired at a step size of 0.5 μm.

Journal of Cell Science • Supplementary information

REAGENT or RESOURCE	SOURCE	IDENTIFIER	remark
Antibodies			Fixation
Guinea pig polyclonal anti-Celsr1	Shi et al., 2014	N/A	4% PFA
Rabbit polyclonal anti-Vangl1	Sigma-Aldrich	Cat# HPA025235; RRID: AB_1858718	4% PFA
Mouse monoclonal anti-α-Tubulin (clone DM1A)	Sigma-Aldrich	Cat#T6199; RRID: AB_477583	4% PFA
Rabbit monoclonal anti-β-Tubulin (clone 9F3)	Cell Signaling Technology	Cat#2128s; RRID: AB_823664	4% PFA
Mouse monoclonal anti-Acetylated-Tubulin (Acetylated-α-Tubulin)	Sigma-Aldrich	Cat#T7451; RRID: AB_609894	4% PFA
Rabbit polyclonal anti-CAMSAP3	Tanaka et al., 2012	N/A	MetOH
Rat monoclonal anti-Odf2	Tateishi et al. 2013	N/A	MetOH
Mouse monoclonal anti-Centriolin (C-9)	Santa Cruz	Cat#sc-365521; RRID: AB_10851483	MetOH
Mouse monoclonal anti-γ-Tubulin	Sigma-Aldrich	Cat#T6557; RRID: AB_477584	MetOH
Rabbit monoclonal anti-γ-Tubulin	Abcam	Cat#ab179503; RRID: N/A	4% PFA
Mouse monoclonal anti-ZO1 (T8-754)	Itoh et al. 1991		MetOH
Goat Alexa488 anti-mouse IgG1	Thermo Fisher Scientific	Cat#A-21121; RRID: AB_2535764	
Goat Alexa488 anti-mouse IgG(H+L)	Thermo Fisher Scientific	Cat#A-11029; RRID: AB_138404	
Goat Alexa488 anti-rabbit IgG(H+L)	Thermo Fisher Scientific	Cat#A-11034; RRID: AB_2576217	
Goat Alexa488 anti-rat IgG(H+L)	Thermo Fisher Scientific	Cat#A-11006; RRID: AB_141373	
Goat Alexa488 anti-guinea pig IgG(H+L)	Thermo Fisher Scientific	Cat#A-11073; RRID: AB_2534117	
Goat Alexa594 anti-mouse IgG1	Thermo Fisher Scientific	Cat#A-21125; RRID: AB_141593	
Goat Alexa594 anti-rabbit(H+L)	Thermo Fisher Scientific	Cat#A-11037; RRID: AB_2534095	
Goat Alexa594 anti-rat IgG(H+L)	Thermo Fisher Scientific	Cat#A-11007; RRID: AB_10561522	
Goat Alexa594 anti-guinea pig IgG(H+L)	Thermo Fisher Scientific	Cat#A-11076; RRID: AB_141930	
Goat STAR580 anti-mouse IgG	Abberior	Cat#2-0002-005-1; RRID: AB_2620153	
Goat STAR635P anti-rat IgG	Abberior	Cat#2-0132-007-5; RRID:N/A	
Chemicals, Peptides, and Recombinant Proteins			
Phalloidin Alexa594	Thermo Fisher Scientific	Cat#A12381; RRID: AB_2315633	
Phalloidin Alexa647	Thermo Fisher Scientific	Cat#A22287; RRID: AB_2620155	
CF®405M Phalloidin	Biotium	Cat#00034; RRID: N/A	
Hoechst33258	Thermo Fisher Scientific	Cat#H3569; RRID: AB_2651133	
Experimental Models: Organisms/Strains			
ICR (female)	Japan SLC	N/A	
Celsr1 mutant mice (female)	Ravni et al., 2009	N/A	
Camsap3 dc/dc mutant mice (female)	Toya et al., 2016	N/A	
B6C3F1 (genetic background of Celsr1 mutant and Camsap3 dc/dc mutant mice)	Japan SLC	N/A	
GFP-Centrin2 Tg mice	Higginbotham et al., 2004	N/A	
Software and Algorithms			
ImageJ	NIH	https://imagej.nih.gov/ij/	
Fiji	Schindelin et al., 2012	https://imagej.net/Fiji	
R	R Core Team (2016)	https://www.r-project.org/	
NIS-Elements	Nikon	http://www.nikon-instruments.jp	
LAS X	Leica	https://www.leica-microsystems.com/	

Table S1. Reagents and resources used in this study

1st antibody	2nd antibody	Excitation	Laser power	Emission	STED	STED laser power	Gate		Fig
Centriolin	STAR580	580nm	10%	590-620nm	775nm	100%		STAR635P→ STAR580 (Between frames)	1, 2C, 4C, 5
Odf2	STAR635P	635nm	10%	655-750nm	775nm	100%			
Centriolin	Alexa488	499nm	10%	504-593nm	OFF	0%		Alexa594 → Alexa488 (Between frames)	3D
CAMSAP3	Alexa594	594nm	10%	603-750nm	660nm	20%	0.3ns-4ns		
CAMSAP3	Alexa594	585nm	10%	590-620nm	775nm	20%		STAR635P→Alexa594 (Between frames)	S2C
Odf2	STAR635P	635nm	10%	655-750nm	775nm	100%			

Table S2. Detailed conditions for STED imaging